# Revealing the strength of three-nucleon interactions with the proposed Einstein Telescope

Henrik Rose,[1] Nina Kunert,[1] Tim Dietrich,[1,2] Peter T. H. Pang,[3,4] Rory Smith,[5] Chris Van Den Broeck,[3,4] Stefano Gandolfi,[6] and Ingo Tews[6]

[1]*Institute for Physics and Astronomy, University of Potsdam, D-14476 Potsdam, Germany*
[2]*Max Planck Institute for Gravitational Physics (Albert Einstein Institute), Am Mühlenberg 1, D-14476 Potsdam, Germany*
[3]*Nikhef, Science Park 105, 1098 XG Amsterdam, The Netherlands*
[4]*Institute for Gravitational and Subatomic Physics (GRASP), Utrecht University, Princetonplein 1, 3584 CC Utrecht, The Netherlands*
[5]*OzGrav: The ARC Centre of Excellence for Gravitational Wave Discovery, Clayton, VIC 3800, Australia*
[6]*Theoretical Division, Los Alamos National Laboratory, Los Alamos, New Mexico 87545, USA*

(Received 23 March 2023; revised 20 June 2023; accepted 28 July 2023; published 22 August 2023)

Nuclear systems, ranging from atomic nuclei to dense matter probed in neutron stars, are governed by strong interactions. Three-nucleon forces have been found to be a crucial ingredient for the reliable description of these systems. Here, we explore how astrophysical data on neutron stars and their mergers from current and next-generation observatories will enable us to distinguish nuclear Hamiltonians. In particular, we investigate two different nuclear Hamiltonians that have been adjusted to reproduce two-nucleon scattering data and properties of light nuclei, but differ in the three-nucleon interactions among neutrons. We find that no significant constraints can be obtained from current data, but that the proposed Einstein Telescope could provide strong evidence to distinguish among these Hamiltonians.

DOI: 10.1103/PhysRevC.108.025811

## I. INTRODUCTION

Neutron stars (NSs) are among the most extreme objects in the universe [1–4] and contain observable matter at the highest densities realized anywhere in nature. Inside NSs, densities up to several times the nuclear saturation density corresponding to $\rho_{\rm sat} \approx 2.7 \times 10^{14}\,{\rm g\,cm^{-3}}$ can be reached. However, the structural properties of typical NSs, i.e., their masses, radii, and deformabilities, are determined to a large extent by dense matter up to 2–3 $\rho_{\rm sat}$. At these densities, neutron-star matter consists mainly of neutrons and protons whose microscopic interactions determine the macroscopic properties of NSs. The macroscopic NS properties can, in turn, be extracted from analyses of data from astrophysical observations, for example gravitational wave (GW) [5–7] and electromagnetic (EM) signals [8–12] from NS mergers, or EM observations of isolated NSs, e.g., from the Neutron Star Interior Composition Explorer (NICER) [13–16]. Hence, by comparing predictions of theoretical models for dense nuclear matter and astrophysical data on typical neutron stars, one can infer properties of microscopic nuclear interactions.

In the previous decade, tremendous progress has been made in calculating the properties of nuclear systems from microscopic nuclear theory. This progress was driven mainly by the development of systematic interactions from chiral effective field theory (EFT) [17,18] as well as improvements to many-body computational methods. These methods solve the many-body Schrödinger equation numerically for a system described by a nuclear Hamiltonian that entails the kinetic energy of the particles as well as their interactions, $\mathcal{H} = T + V_{\rm NN} + V_{\rm 3N} + \cdots$, where $V_{\rm NN}$ denotes two-nucleon (NN) interactions, $V_{\rm 3N}$ denotes three-nucleon (3N) interactions, and the dots indicate additional many-body forces. Calculations of properties of atomic nuclei and isotopic chains [19,20] and studies of nuclear matter [21–23] have shown that 3N interactions are an important ingredient in nuclear Hamiltonians and crucial to accurately describe data.

In chiral EFT, 3N interactions are usually constructed to reproduce properties of light nuclei [24–26] and then used to study heavier atomic nuclei and neutron-rich matter relevant for astrophysics. The latter requires the extrapolation of these interactions from nearly symmetric to almost pure neutron systems, which might suffer from systematics if interactions among neutrons are poorly constrained. Hence, it is desirable to investigate if one can constrain these interactions directly in neutron-rich systems. In this paper, we examine how well we can distinguish between nuclear Hamiltonians that include different 3N interactions by analyzing GW signals of NS mergers, fully taking into account present uncertainties in nuclear theory. We probe how different tidal properties, due to the different 3N contributions, can be extracted from a catalog of synthetic signals as observed in future third-generation detectors, e.g., the Einstein Telescope (ET) [27,28].

## II. METHODS

### A. Equations of state for different three-nucleon interactions

To analyze the impact of 3N interactions on the equation of state (EOS) of NSs, we follow Ref. [29] and construct two EOS sets constrained by auxiliary field diffusion Monte Carlo calculations [30–32] of pure neutron matter for two local

 

Hamiltonians from chiral EFT [33–35]. These Hamiltonians differ in their 3N interactions in pure neutron matter [the interactions of Ref. [35] named two-pion exchange (TPE) and $V_{E,\mathbb{1}}$[1]], but they give a similar description in atomic nuclei [36].

The difference in the neutron-matter description originates from regulator artifacts in the EOS due to the 3N contact interaction $V_E$ [35]. In pure neutron matter, without any regulators, the TPE interaction is the only 3N contribution because the shorter-range one-pion-exchange–contact interaction $V_D$ and 3N contact $V_E$ vanish due to their spin-isospin structure and the Pauli principle, respectively [37]. However, when local regulators are applied, the contact interactions acquire a finite range and start to contribute also to pure neutron systems [35,38]. Here, we use these regulator artifacts to our advantage to test the sensitivity of the EOS to different 3N interactions.[2] The first Hamiltonian only contains the TPE interaction, while the second Hamiltonian additionally contains a repulsive 3N contact piece with the identity operator, $V_{E,\mathbb{1}}$.

For both Hamiltonians, we calculate the EOS up to $2\,\rho_{\rm sat}$ and estimate the truncation uncertainties according to the description used in Ref. [35]. We stress that this choice for the upper EFT density is less conservative but will enable us to demonstrate more clearly the impact of third-generation detectors. We extend these calculations to beta equilibrium and include a crust following the description of Ref. [39]. This crust model includes EFT uncertainties. We translate this to a band in the density–speed-of-sound plane from which we sample 3000 low-density EOSs for each Hamiltonian. For simplicity, we refer to the two sets as TPE and $V_{E,\mathbb{1}}$, too. We can then extend each of them to higher densities using the speed-of-sound extrapolation scheme introduced in Ref. [29]. For the extension, the prior in the radius of a typical $1.4\mathrm{M}_\odot$ NS is "natural," i.e., we directly use the generated EOSs as prior and do not postselect EOSs to generate a certain prior shape. Hence, both EOS sets enable us to explore the impact of different 3N interaction strengths while taking into account all theoretical uncertainties.

Including these uncertainties is key in answering the question of whether current and future observations can distinguish between nuclear Hamiltonians and, in our case, can reveal the strength of 3N interactions. First, uncertainties in the nuclear EOS are not solely originating from unknown 3N interactions, which is reflected by the truncation uncertainty separately estimated for each Hamiltonian employed here. Second, at higher densities in the core of NSs, a description in terms of nucleonic degrees of freedom alone might fail as exotic forms of matter might appear. Using the speed-of-sound extrapolation allows us to account for all possible density behavior at high densities. Both uncertainties soften the constraining power of multimessenger data but are crucial to make robust statements about prospects of constraining nuclear Hamiltonians.

[1]We do not investigate the $V_{E,\tau}$ interaction of Ref. [35] because it leads to negative pressure in pure neutron matter below $2\rho_{\rm sat}$.

[2]In principle, these regulator artifacts can be thought of as subleading 3N contact interactions, appearing first at N$^4$LO in chiral EFT.

Our approach, thus, differs significantly from Refs. [40,41], which first investigated the impact of GW measurements with current and future GW detectors on inferring 3N forces in the nuclear Hamiltonian. In contrast to our paper, Refs. [40,41] employed phenomenological NN and 3N Hamiltonians and constructed a set of EOSs by varying one parameter that quantifies the strength of the phenomenological 3N contact potential. Here, instead, we use two realistic nuclear Hamiltonians based on chiral EFT that are both adjusted to reproduce experimental data on atomic nuclei and for which we can estimate theoretical uncertainties. Furthermore, Refs. [40,41] assumed their nuclear models to be valid throughout the whole density range of NSs, neglecting the possibility of changes to the high-density equation of state due to novel phases of matter. We, instead, include such uncertainties by using a general EOS extension scheme. Finally, they assumed a noise-free realization of GW measurements in their injection campaign, whereas we include detector noise.

### B. Injection campaign

The EOS links to GW measurements of NS mergers due to tidal deformations of the stars during the inspiral phase. This leaves a characteristic imprint on the observable gravitational waveform [42]. It is most commonly expressed by the (effective) tidal deformability

$$\tilde{\Lambda} := \frac{16}{13}\frac{(M_1 + 12M_2)M_1^4\Lambda_1 + (1 \longleftrightarrow 2)}{(M_1 + M_2)^5}, \qquad (1)$$

a mass-weighted average of both components' tidal deformability $\Lambda := \frac{2k_2R^5}{3M^5}$. Here $k_2$ denotes the tidal Love number which, like the radius $R$, depends on the EOS [43]. Together with the component masses $M_i$, the EOS is therefore sufficient to determine $\tilde{\Lambda}$. Conversely, $M$-$\Lambda$ and $M$-$R$ relations directly map back to the EOS. Three-nucleon interactions increase the pressure in the EOS, leading to an increase in the tidal deformability compared to NN interactions only. As different 3N interaction models do this to a different degree, we can use information on the tidal deformability to constrain 3N forces. The EOSs in the $V_{E,\mathbb{1}}$ set are stiffer at low densities due to the additional repulsion term in the nuclear Hamiltonian. This usually leads to a larger radius at low masses and the stars are more susceptible to deformations, i.e., we generally expect to observe a higher $\tilde{\Lambda}$ than for the softer TPE set. Four-nucleon forces, on the other hand, have been shown to be small and can safely be neglected [44,45]. The contour lines in Fig. 1 indicate the 50 and 90% range of both $M$-$\Lambda$ and $M$-$R$ relations allowed by either EOS set.

A reanalysis of the GW transient GW170817 with respect to 3N interactions proves uninformative, though (see Appendix A for details). In principle, the EOS is linked to EM observables, too, as it determines NS radii and, thus, affects the properties of ejected matter. Intricate models of this connection to EM counterparts are under development, but current uncertainties do not allow stringent constraints on 3N interactions. These modeling efforts will profit from additional multimessenger events observed with the present detector generation [46,47]. Yet event rates are highly

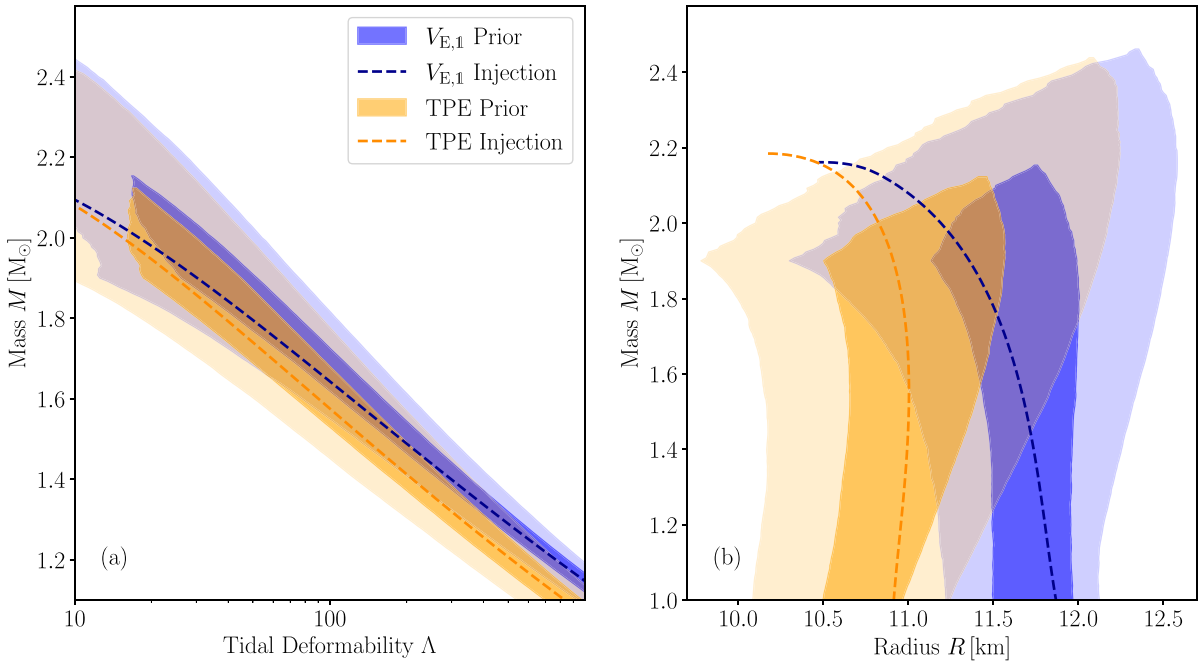


FIG. 1. $M$-$\Lambda$ (a) and $M$-$R$ relation (b) for EOS prior and injections. Shaded bands indicate regions in prior space covered by 90 and 50% of EOSs, respectively. The two sets are well distinguishable at low masses. As central densities and masses rise, smaller sections of the stars are governed by the EFT regime and the parameter spaces increasingly overlap by construction. The injected EOS from each set (dashed lines) is therefore chosen based on the $\Lambda$distribution at a relatively low mass of $1.2\,M_\odot$. We inject the EOS from the distribution's 50th percentile which has a TOV mass closest to a fiducial value of $2.2\,M_\odot$.

uncertain and kilonova rates are especially poorly constrained [48–51]. We conclude that significantly improved constraints may not be expected before future detector technology becomes operational [52]. In the GW sector, this refers to the third-generation ET [27] in Europe and the proposed Cosmic Explorer (CE) [53] in the US. We, therefore, explore synthetic GW signals detected with ET. To that end, we choose an example EOS for both Hamiltonians and perform a volume-limited injection study that analyzes 20 realistic NS mergers [3]. For each injected signal, we compare Bayesian parameter estimation over the TPE and $V_{E,\mathbb{1}}$ set, amounting to a total of 80 inference runs. Subject to the population model under consideration, the detection of 20 such systems will amount to at least two years of observations at ET [54,55].

The injected component masses $M_{1,2}$ are drawn from a Gaussian distribution $\mathcal{N}(\mu = 1.33, \sigma = 0.09)$ that is characteristic for galactic binary NS (BNS) systems [3]. They cover a range from $1.14\,M_\odot$ to $1.53\,M_\odot$. The systems are uniformly distributed in a comoving volume with a distance cutoff at 200 Mpc. In a larger random sample of 1000 binaries within 500 Mpc, the detections' average chirp mass settles at this distance near the injected distribution's mean, indicating that the volume is sufficiently large to characterize the underlying distribution. We further limit our analysis to systems with a signal-to-noise ratio (SNR) above 30. This value is sufficiently high to expect measurements of significant tidal contributions without introducing a bias towards higher masses, where tidal effects would again become less prominent. The dimensionless aligned spins $\chi_{1,2}$ are constrained to a uniform distribution subject to $|\chi_i| < 0.05$, as implied for realistic sources of NS mergers [56,57]. We leave the sky location (declination and right ascension), inclination angle $\theta_{JN}$, orbital phase at coalescence $\phi$, and polarization angle $\psi$ totally unconstrained.

From our two EOS sets, we select one EOS each for the injection campaigns with 20 binaries according to the following considerations. We naturally expect to obtain the strongest constraints on 3N interactions from low-mass binaries because the densities explored in these systems are closer to the densities that can comfortably be described by nucleonic models of matter. They are, therefore, more influenced by the EFT calculations and less so by the high-density extrapolations. Figure 1 shows how the parameter spaces of the EOS sets largely overlap at high masses, corresponding to core densities far beyond the breakdown of the chiral EFT approach. In order to minimize biases resulting from the choice of injection EOS, we base our selection on both sets' associated $\Lambda$ distribution at a relatively low mass of $1.2\,M_\odot$. This mass is supported by observations and neutron star formation theories [58,59]. We then choose to inject the EOS from each distribution's 50th percentile which has a Tolman-Oppenheimer-Volkoff (TOV) mass[3] closest to a fiducial value of $2.2\,M_\odot$. In that sense, the chosen EOS is representative for its EFT Hamiltonian in a low-mass regime and it is sufficiently realistic at high masses. We use the IMRPHENOMD_NRTIDALV2 approximant to

[3]The TOV mass is the limiting mass above which the neutron star structure equations have no stable solution.

TABLE I. GW sampling parameters in the ET analysis. Most priors are uniform within given bounds. The declination $\delta$ is uniform in cosine, and the luminosity distance $d_{\rm L}$ is uniform within a comoving volume of the specified dimension. The EOS prior is weighted by the ability to support massive pulsars. Prior ranges in italics indicate constraints that are not used as sampling parameters. Starred priors are adjusted to the injected signal.

| Parameter | Symbol | Prior bounds |
|---|---|---|
| Observational | | |
| Luminosity distance (Mpc) | $d_{\rm L}$ | 5, 500 |
| Inclination | $\cos\theta_{JN}$ | $-1$, 1 |
| Phase (rad) | $\phi$ | 0, $2\pi$ |
| Polarization (rad) | $\psi$ | 0, $\pi$ |
| Right ascension (rad) | $\alpha$ | 0, $2\pi$ |
| Declination (rad) | $\delta$ | $-\pi$, $\pi$ |
| Orbital | | |
| Chirp mass ($M_\odot$) | $\mathcal{M}$ | *1.20, 1.30** |
| Source chirp mass ($M_\odot$) | $\mathcal{M}_s$ | 1.15, 1.30* |
| Mass ratio | $q$ | 0.125, 1 |
| Source component mass ($M_\odot$) | $M_{i,s}$ | *>0.5* |
| Aligned component spin | $\chi_i$ | $-0.15$, 0.15 |
| Hyper | | |
| Equation of state | EOS | 1, 3000 |

generate a measurable gravitational wave from these parameters in the frequency range 30 to 2048 Hz [60]. This is then superposed by random detector noise to simulate a realistic GW strain in ET.

### C. Parameter estimation

We analyze the resulting strain in the framework of Bayesian inference. This makes use of Bayes' theorem,

$$p(\theta|d) = \frac{L(d|\theta)\pi(\theta)}{\mathcal{Z}(d)}, \text{ with} \tag{2}$$

$$\mathcal{Z}(d) = \int_\Theta L(d|\theta)\pi(\theta)\,d\theta, \tag{3}$$

to determine a posterior distribution $p(\theta|d)$ in the multidimensional parameter space $\Theta$ that characterizes an event's GW signal. We obtain the posterior by reweighting a parameter set's prior probability $\pi(\theta)$ by the likelihood $L$ that the parameter set describes the data $d$. In the context of GW analyses, we determine how well a waveform model computed from various input parameters matches the observed GW strain. The likelihood evaluations follow the usual matched filter approach with the IMRPHENOMD_NRTIDALV2 approximant to efficiently and robustly generate waveforms including tidal effects [60]. Because this reweighting cannot be done analytically, we have to resort to a statistical approximation by numerically sampling over $\Theta$. The sampling parameters that describe the waveform space of our injection study are given in Table I.

These include observational parameters (e.g., luminosity distance $d_{\rm L}$, phase, inclination angles of the merger) and intrinsic binary parameters (e.g., chirp mass $\mathcal{M}$, mass ratio, tilts). We considerably extend the range above the injection distribution for the luminosity distance and aligned spins in order to avoid boundary effects from the prior distribution. This comes at the cost of a bias towards unequal mass ratios in the parameter estimation, though. As stated above, each EOS uniquely defines the tidal deformabilities, which are required as input to the waveform approximant, for any given component mass. We can, therefore, use the EOS as a sampling parameter that is constrained by tidal terms in the observed waveform. The EOS prior is weighted conservatively by incorporating a lower bound on the TOV mass in agreement with precise pulsar observations [61–63] (compare Fig. S1 of Ref. [12]).

In order to reduce the significant computational cost of waveform evaluations during the likelihood computation, we apply a reduced-order-quadrature (ROQ) rule [64]. This requires limiting the chirp mass space to $0.1\,M_\odot$ intervals. ROQs apply to the observed signal and hence to mass parameters as seen in a detector frame. It is redshifted against the source frame of the system, whose nonredshifted masses determine the tidal effects. As we sample over chirp masses in the source frame, we invoke a corresponding prior adapted to the injected signal in order to avoid computational issues. Since the chirp mass is by far the most accurately measured quantity, the prior is still wide enough to avoid the introduction of prior-driven artifacts in the parameter estimation.

Due to this high dimensionality of the GW parameter space, parameter estimation is a computationally challenging problem for which we use nested sampling [65,66]. Nested sampling algorithms aim at calculating the evidence $\mathcal{Z}$ and yield the posterior *en passant*. We employ the implementation of PARALLEL-BILBY with 2048 live points [67]. This is an efficient parallelization package relying on nested sampling routines from BILBY [65,68], with some minor modifications to accommodate EOS sampling. The frequency range of 30 to 2048 Hz is chosen to reduce computational costs with signals lasting less than 2 min.[4] In this setting, each inference run requires about 80 000 h of computing time.

### D. Model selection

The big advantage of nested sampling is that we can use it not only for parameter estimation, but also for model selection. This relies on the observation that a higher evidence $\mathcal{Z}$ can only be achieved by the more complex (i.e., with a less compact prior $\pi$) among two competing models if it matches the data significantly better. Treating both models of 3N interaction beforehand as equally likely, we follow common practice to express model preference for the TPE or $V_{E,\mathbb{1}}$ Hamiltonians by a Bayes factor $\mathcal{B}^{V_{E,\mathbb{1}}}_{\rm TPE} = \frac{\mathcal{Z}_{V_{E,\mathbb{1}}}}{\mathcal{Z}_{\rm TPE}}$ or its logarithm $\ln \mathcal{B}^{V_{E,\mathbb{1}}}_{\rm TPE} = \ln \mathcal{Z}_{V_{E,\mathbb{1}}} - \ln \mathcal{Z}_{\rm TPE}$. Moreover, the strength of 3N

[4]While tidal effects are hardly measurable before, ET will certainly be able to detect a GW signal below 10 Hz. From this frequency range, most information on other GW parameters can be obtained [69]. We discuss the consequences of this choice in Sec. III B.

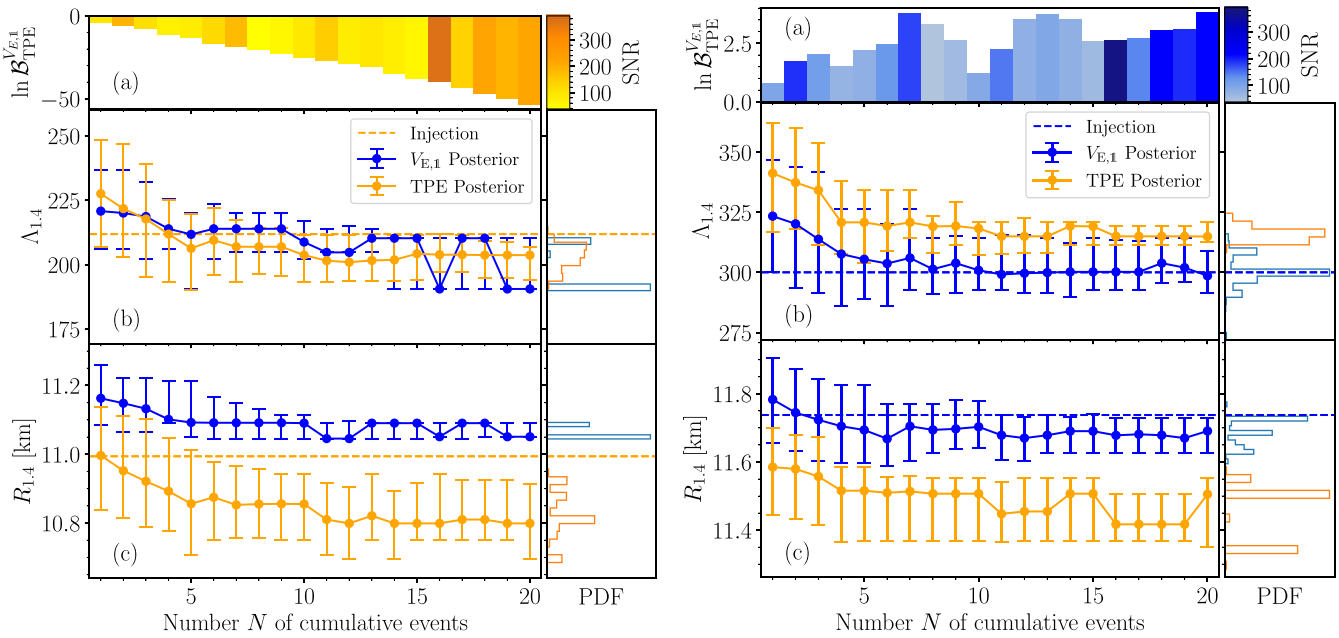


FIG. 2. Joint EOS posteriors and Bayes factors. For a TPE (left) and $V_{E,\mathbb{1}}$ (right) injection, we show model preference as expressed by a cumulative Bayes factor (a), color coded by the event's SNR. While the evidence in favor of a TPE injection piles up almost linearly, some runs with low SNR disfavor the $V_{E,\mathbb{1}}$ set when injected. Below, we show for each injected EOS the results of parameter estimation with both EOS sets. Joint posteriors on the observable tidal deformability $\Lambda$ (b) and radius $R$ (c) of a $1.4\,\mathrm{M}_\odot$ NSs are displayed as a function of total signals observed in random order. The smaller windows show the same posteriors as a probability density function (PDF) after all 20 events.

interactions is a universal property. The evidence for either model explaining a suite of $N$ independent observations is given by

$$\mathcal{Z} = \int \prod_{i=1}^{N} L_i(\theta_i, \mathrm{EOS}_i)\pi(\theta_i, \mathrm{EOS}_i)\, d\theta_i d\mathrm{EOS}_i \tag{4}$$

$$= \prod_{i=1}^{N} \int L_i(\theta_i, \mathrm{EOS}_i)\pi(\theta_i, \mathrm{EOS}_i)\, d\theta_i d\mathrm{EOS}_i \tag{5}$$

$$= \prod_{i=1}^{N} \mathcal{Z}_i. \tag{6}$$

This has subsumed all system parameters besides the EOS in $\theta_i$. The corresponding Bayes factor

$$\mathcal{B}^{V_{E,\mathbb{1}}}_{\mathrm{TPE}} = \prod_{i=1}^{N} \frac{\mathcal{Z}_{V_{E,\mathbb{1}},i}}{\mathcal{Z}_{\mathrm{TPE},i}} \tag{7}$$

then expresses the statistical support for the notion that the $N$ systems are characterized by the $V_{E,\mathbb{1}}$ description instead of TPE.

We highlight that this is a statement on the EOS *set* and hence the 3N interactions we explore, not on the EOS itself. In principle, all neutron stars should be described by the same EOS. This assumption is built into our EOS sampling because the algorithm always tests one EOS on both stars. We may therefore treat the EOS as a hyperparameter and derive a joint posterior $p(\mathrm{EOS})$. Its distribution after observing $N$ systems is given by

$$p(\mathrm{EOS}) = \mathrm{const}\frac{\prod_{i=1}^{N} p_i(\mathrm{EOS})}{\pi(\mathrm{EOS})^{N-1}}, \tag{8}$$

with $p_i(\mathrm{EOS})$ denoting the posterior distribution obtained from the $i$th event, marginalized over all parameters but the EOS. We can use this to define posteriors of EOS-associated quantities, e.g., a $1.4\,\mathrm{M}_\odot$ NS's radius $R_{1.4} := R(\mathrm{EOS}, M = 1.4\,\mathrm{M}_\odot)$ or tidal deformability $\Lambda_{1.4} := \Lambda(\mathrm{EOS}, M = 1.4\,\mathrm{M}_\odot)$. However, one needs to be cautious when including this knowledge in the computation of Bayesian evidence for either EOS model. The EOS parameter space conveys present modeling uncertainties in nuclear theory. This leads to unequal prior densities in the associated observables. Hence, an EOS set of which only one model EOS survives after the inference might be erroneously favored over a set where multiple EOSs remain. We further discuss this subtlety in Appendix B.

## III. RESULTS

### A. Population analysis

Combining the information from each event into a cumulative EOS posterior using Eq. (8) and a joint model evidence using Eq. (6), we obtain the results illustrated in Fig. 2. On the left, we show the EOS posterior—expressed by the observable tidal deformability $\Lambda_{1.4}$ (middle) and the radius $R_{1.4}$ (bottom) of a fiducial $1.4\,\mathrm{M}_\odot$ NS—for both EOS sets when injecting a TPE EOS. Evidence in favor of the TPE Hamiltonian accumulates very quickly and essentially independent of further system parameters (top). Particularly, we see no correlation

with the color-coded SNR. We obtain $\ln \mathcal{B}^{V_{E,\mathbb{1}}}_{\mathrm{TPE}} = -53.5 \pm 1.3$ after all 20 mergers, i.e., strong preference for the injected TPE model, although the injected EOS has only 0.04% weight in the joint TPE posterior.

Some considerations are in order to properly interpret these findings. As an increasing amount of observations is made, the TPE posterior (orange) narrows down continuously and the median estimate for $\Lambda_{1.4}$ decreases until it settles at $\Lambda_{1.4,\mathrm{TPE}} = 204^{+4}_{-10}$ (90% CI). This falls just below the corresponding injection value $\Lambda_{1.4,\mathrm{inj}} = 212$. In contrast, the posterior obtained from individual runs typically overestimates the injected tidal deformability. This relates to our conservative prior choice which only penalizes low TOV masses. EOSs that allow for higher TOV masses are typically associated with higher $\Lambda$ values, too. Individual runs are therefore biased towards overestimates of $\Lambda$ at any reference mass. The joint estimate approaches a more realistic limit only as data from more runs and a wider range of component masses is included.

That the injection value is not recovered within 90% CI of the joint posterior is primarily due to a systematic overestimate of the luminosity distance $d_{\mathrm{L}}$ or, equivalently, the redshift. The observed mass parameters are degenerate in redshift, while $\Lambda$ is determined by the component masses in their source frame (i.e., not redshifted). The overestimate in $d_{\mathrm{L}}$ leads to an underestimate of these masses. Low masses correspond to higher deformability, an effect that the sampling algorithm will naturally compensate by selecting EOSs of more compact NSs to match the measured tidal effects. The even larger underestimate of a $1.4\,\mathrm{M}_\odot$ NS's radius with $R_{1.4,\mathrm{TPE}} = 10.80^{+0.12}_{-0.10}\,\mathrm{km}$ is aided by the fact that our injection EOS happens to exhibit the highest radius ($R_{1.4,\mathrm{inj}} = 11.0\,\mathrm{km}$) among the EOSs that live in a narrow $\Lambda$band around the injection value at $1.4\,\mathrm{M}_\odot$. As observations of the inspiral signal are not radius sensitive, and we would thus expect a radius underestimate even if we had observed a more accurate $\Lambda$ recovery. This highlights the fact that the NS radius and its tidal deformability are not fully equivalent quantities.

Similar arguments apply to the overall trend in the $V_{E,\mathbb{1}}$ posterior (blue). It overestimates the tidal deformability at the reference mass $1.4\,\mathrm{M}_\odot$ for individual runs and decreases as we include data from additional observations. However, the overall capability of this set to explain the injected TPE signals is very low. The soft injection covers a low-$\Lambda$ regime that is only sparsely populated by the on-average stiffer $V_{E,\mathbb{1}}$ EOSs. It requires a very peculiar extrapolation in the high-density end for a $V_{E,\mathbb{1}}$ EOS to soften sufficiently already for medium-mass stars to provide decent agreement with the TPE injection while still allowing for a sufficiently high TOV mass. This explains the strong preference for the TPE Hamiltonian. The tighter and better fit of the $V_{E,\mathbb{1}}$ posterior therefore must not be mistaken for evidence of better agreement with the observational data. To the contrary, this indicates the narrow range and low number of EOSs that provide a mildly plausible description of the data. After the 13th detection, only two EOSs populate more than 90% of the $V_{E,\mathbb{1}}$ posterior space and cause the apparent jumps of the observables' median estimate. The seemingly better agreement with the injection, particularly for $R_{1.4}$, should therefore not lead us astray: the ET's high resolution effectively rules out $V_{E,\mathbb{1}}$ after a sufficient amount of signals.

Conversely, the corresponding plot for the $V_{E,\mathbb{1}}$ injection on the right of Fig. 2 demonstrates a much weaker model preference at $\ln \mathcal{B}^{V_{E,\mathbb{1}}}_{\mathrm{TPE}} = 3.8 \pm 1.3$ (top, note the different scales). This links to the fact that the TPE model naturally provides better support for the $V_{E,\mathbb{1}}$ set's $\Lambda$ distribution than vice versa: As the $V_{E,\mathbb{1}}$ set is characterized by higher tidal deformability at lowest masses, the injected $\Lambda$ values are then best matched by EOSs in the TPE set that stiffen considerably and early on in comparison to the full prior. These are likely to yield high TOV masses which our prior does not penalize due to the lack of confidently measured upper bounds, in contrast to the softening $V_{E,\mathbb{1}}$ EOSs in case of the TPE injection.

The six events with the lowest SNR even seem to favor the TPE model to various degrees. A low SNR in the considered distance range is typically related to low inclination angles. Due to the well-known inclination-distance degeneracy, these systems are especially prone to overestimates of the luminosity distance. In the apparent source frame, component masses appear then lower than injected. If we knew the true EOS, we could use tidal deformability measurements to break this degeneracy. But as we explore the EOS, these observations erroneously indicate a soft EOS which favors the TPE model.

Nevertheless, the joint $V_{E,\mathbb{1}}$ posterior after all runs is at $\Lambda_{1.4,V_{E,\mathbb{1}}} = 299^{+10}_{-7}$ in good agreement with $\Lambda_{1.4,\mathrm{inj}} = 300$ (dashed line), while the TPE posterior overestimates it at $\Lambda_{1.4,\mathrm{TPE}} = 315^{+6}_{-3}$. Figure 3 illustrates the reason for this. It shows the ten most likely EOSs from each set together with the $V_{E,\mathbb{1}}$ injection. Fainter lines correspond to subdominant posterior contributions and background contours match the prior ranges (90% CI) in $\Lambda$ (left) as well as radius (right). Since merging binaries form a distinct subpopulation of all NSs, our injection was guided by the mass distribution of galactic BNS systems. We see that $\Lambda$ is best recovered around that distribution's mode at $1.33\,\mathrm{M}_\odot$ [3]. TPE EOSs matching this value despite their lower deformability at low mass "overshoot" the $V_{E,\mathbb{1}}$ injection in the $M$-$\Lambda$ plane above $1.33\,\mathrm{M}_\odot$. That the joint TPE posterior overestimates $\Lambda_{1.4}$ is therefore indicative of the probed mass range. It does not contradict the fact that TPE provides in general softer EOSs. The latter is further indicated by the lower radius estimate in case of the TPE model. Here, too, the final posterior is dominated by a very low number of remaining EOSs.

### B. Validation

As we have discussed above, the lack of symmetry in the degree of model preference for the respective injection is linked to our prior choice. The $V_{E,\mathbb{1}}$ model's ability to reproduce the TPE injection is limited due to the prior penalty on low TOV masses. However, there is some evidence for the formation of a short-lived hypermassive NS in the GW170817 merger [70–73]. Its rapid collapse to a black hole would be in conflict with the most preferred TPE EOSs in case of the $V_{E,\mathbb{1}}$ injection. We see in the mass-radius plot in Fig. 3 that these EOSs mostly have TOV masses of $2.4\,\mathrm{M}_\odot$ and above. While we consider a maximum limit on the TOV mass too

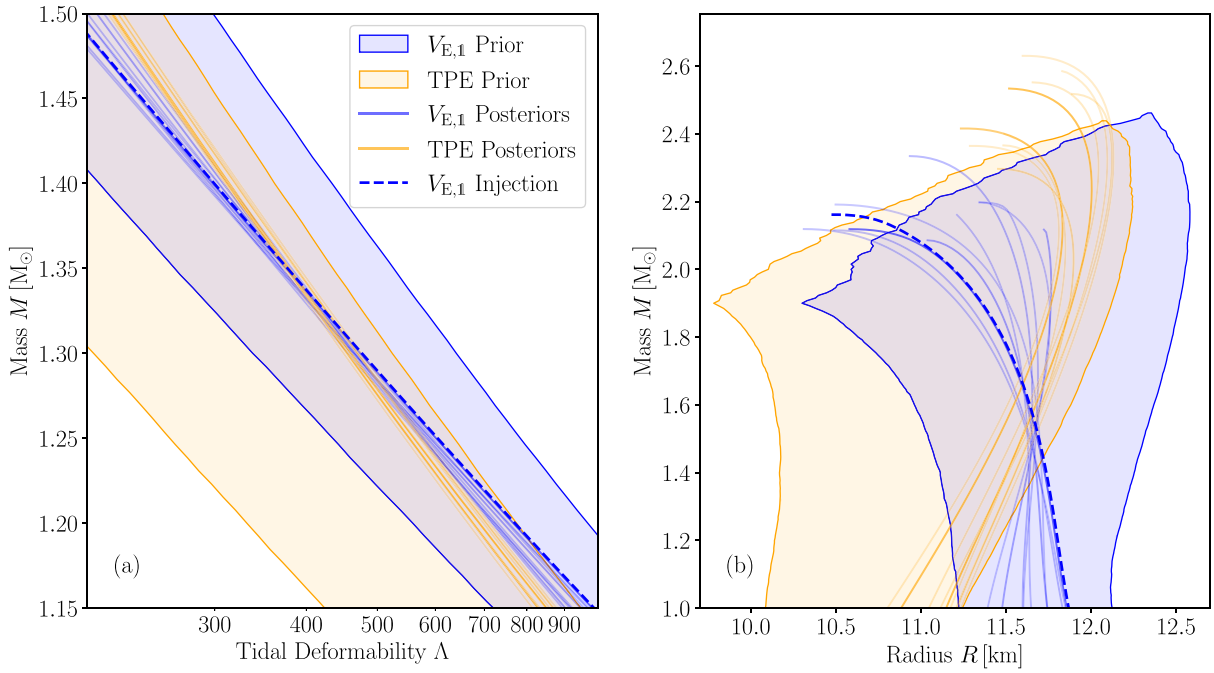


FIG. 3. $M$-$\Lambda$ (a) and $M$-$R$ relation (b) for EOS prior and posterior. Similar to Fig. 1, shaded bands indicate regions in prior space covered by 90% of EOSs. We show the $V_{E,\mathbb{1}}$ injection as a dashed line alongside the ten dominant EOSs in each set's corresponding posterior. Note how the tidal deformability is best constrained around the mean mass of the underlying mass distribution.

uncertain at the moment to include it in our more conservative main analysis, we acknowledge that new observations could provide a more confident upper limit on this mass. A corresponding penalty in the EOS prior could reduce the erroneous TPE preference and shift the Bayes factor in favor of the injection. We therefore reanalyze a signal with particularly poor parameter estimation in the $V_{E,\mathbb{1}}$ injection, using a different EOS prior that additionally penalizes TOV limits above $2.16^{+0.17}_{-0.15}\,M_\odot$ [70]. This step does not significantly improve the $V_{E,\mathbb{1}}$ estimation for observable parameters, while it does lead to a modified EOS posterior. The TPE sampling, in contrast, does not converge within acceptable runtime because the adjusted prior effectively outlaws EOSs that previously provided suitable waveform descriptions. This makes it much harder for the nested sampling algorithm to find parameters with better likelihood. Enforcing convergence by allocating significantly more computing resources would certainly have removed the model preference for TPE against the injection.

Significantly better data will be available in real observations. We based our analysis on observations above 30 Hz where tidal effects begin to contribute. Inference on the full detection band would have further increased the high computational cost of this study by orders of magnitude. The mass and spin parameters of a compact binary, however, are best determined at 5 to 9 Hz in ET [69]. Measuring them with high precision in this range would naturally constrain the inference of other parameters, too. Similarly, a signal recorded by a GW detector network or even identified in optical counterparts would constrain the sky localization to be much tighter. To mimic these effects, we reanalyze the same signal with our usual priors, but under the assumption that (a) mass parameters and sky location were tightly constrained, as expected from a full bandwidth detection in a GW detector network, and (b) the luminosity distance was known to high precision, as expected from the identification of the host galaxy to an EM counterpart.

Figure 4 shows that option (a) already leads to a more accurate description of the tidal effects. In our original analysis, the distance overestimate drives the EOS sets to EOSs with lower tidal deformability to counter the underestimate in the (redshifted) source-frame mass parameters. These are associated with more compact neutron stars that typically have a lower TOV limit. Because our prior penalizes low TOV limits, good waveform fits had previously worse prior support, particularly for $V_{E,\mathbb{1}}$. Properly identifying the detected mass within narrow margins of $0.01\,M_\odot$ reduces this source of uncertainty considerably and resolves the erroneous model preference for TPE against the injected $V_{E,\mathbb{1}}$ EOS. Constraining the luminosity distance even further in (b), for instance by identifying a host galaxy, does not improve the estimation of other parameters and in particular $\tilde{\Lambda}$. These findings support the conclusion that realistic GW detections in the ET era with improved priors from upcoming detections will be capable of quickly distinguishing 3N interactions.

### C. Discussion

Our analysis comes with some caveats. First, Ref. [74] has shown in a comparable framework how systematic errors in available waveform approximants affect the determination of tidal effects. Given the greatly increased sensitivity of ET and the prospect of advances in waveform modeling in the

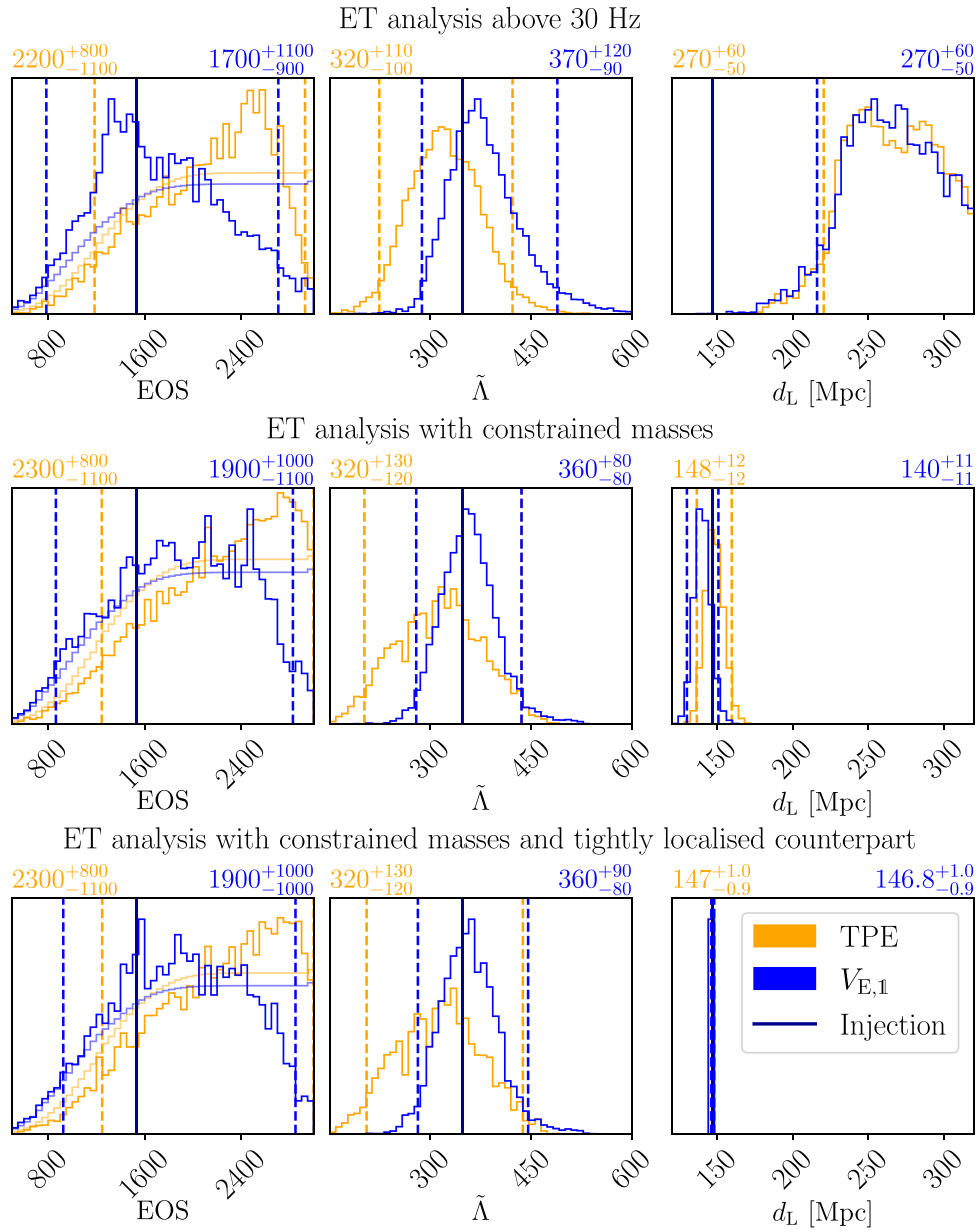


FIG. 4. Selected posteriors with adapted priors. We show the posteriors for the EOS indices (left), the associated tidal deformability (center), and luminosity distance (right) in our original setup (top), with tightly constrained mass parameters as expected from realistic network operation (middle), and with known distance as expected from the localization of an EM counterpart (bottom). The fainter lines in the EOS plots indicate the indices' prior weight. Note how the distance estimate and the tidal description improve when assuming knowledge on the mass parameters. Further limiting the luminosity distance does not improve the quality of other parameters.

upcoming years, we are optimistic that these uncertainties will be reduced significantly when analyzing future detections.

Second, we have drawn the component masses from a $\mathcal{N}(\mu = 1.33, \sigma = 0.09)$-distributed population. In principle, the impact of three-nucleon interactions on the observable structure is strongest for low masses, and high-mass systems will be less constraining. The relatively tight distribution from which we have drawn masses is based on observations of close NS binaries in the milky way. Its difference to the mass distribution of isolated NSs indicates peculiar formation channels which benefit our paper [75]. The fact that the only other confidently measured NS merger GW190425 contained at least one component with significantly higher masses could indicate selection effects in current radio surveys and the underestimation of other formation channels in population evolution studies [76,77]. Nevertheless, a higher fraction of massive NSs does not harm our analysis: It would only take longer to reach a desired level of confidence with less constraining high-mass mergers. Moreover, for the low- to medium-mass range of our paper, we found the quality of

the strain (i.e., SNR) to outweigh effects due to the component masses.

Third, our analysis naturally depends on the true EOS, too. If it exhibited extremely low (or high) tidal effects that the $V_{E,\mathbb{1}}$ (or TPE) model cannot reproduce, the amount of detections necessary to reach a desired level of model preference will drastically reduce. If, by contrast, the true EOS covered just the middle of both models' associated $M$-$\Lambda$ space, a misidentification could only be avoided by studying extremely low-mass systems or by employing more advanced modeling.

## IV. CONCLUSIONS

We have performed an ET injection study to investigate if future GW observations can help to constrain the nuclear Hamiltonian in NS matter. For our TPE and $V_{E,\mathbb{1}}$ injection choices, constrained by chiral EFT at low densities and observations at high densities, we have found $\ln \mathcal{B}^{V_{E,\mathbb{1}}}_{\mathrm{TPE}} = -53.5 \pm 1.3$ and $3.8 \pm 1.3$, respectively. The strength of model preference will naturally change for more or less extreme EOSs as well as for denser EOS sets.

These outcomes need to be seen in context of computational limitations and our rather conservative approach. We performed inference on the frequency domain above 30 Hz to limit this study's computational cost. While tidal terms are hardly distinguishable below, this has in fact cut the most promising information on the mass parameters which contribute most information in ET around 5 to 9 Hz [69]. Additionally, we have only taken a detection by ET alone into consideration. Network operation with CE and other GW detectors as well as sky localization by detection of EM counterparts would greatly improve inference on GW parameters, including the luminosity distance, under realistic conditions and reduce the observed bias towards the TPE model. Moreover, upper limits on the TOV mass will be refined by further multimessenger detections of NS mergers. We can therefore be optimistic to achieve significantly better constraints in actual science runs. That we have not recovered our injected EOSs in our inference runs, but closely similar models, reminds us that we only probe the limited mass range of merging NSs. While we will be able to mitigate some systematic effects by taking into account other aspects of the expected multimessenger signals, we cannot expect to fully recover our injections.

However, even under our conservative assumptions, we found clear evidence in support of either injected Hamiltonian, particularly when considering the systems with high SNR. This suggests that observations with third generation GW detectors alone will be able to amass the required data to decisively distinguish nuclear Hamiltonians. Joint detections then reduce the amount of necessary events to surpass a desired level of confidence, underlining the potential of multimessenger astronomy to inform nuclear theory. Naturally, if the true EOS proves more extreme, our results will be more constraining than if the true EOS can be described well by either Hamiltonian. Notwithstanding, our approach is not limited to 3N interactions but can in principle be used to constrain other parts of the Hamiltonian, too.

## ACKNOWLEDGMENTS

The work of S.G. and I.T. was supported by the U.S. Department of Energy, Office of Science, Office of Nuclear Physics, under Contract No. DE-AC52-06NA25396; by the U.S. Department of Energy, Office of Science, Office of Advanced Scientific Computing Research, Scientific Discovery through Advanced Computing NUCLEI program; and by the Laboratory Directed Research and Development program of Los Alamos National Laboratory under Project No. 20230315ER. The work of S.G. was also supported by the Department of Energy Early Career Award Program. The work of I.T. was also supported by the Laboratory Directed Research and Development program of Los Alamos National Laboratory under Project No. 20220541ECR. This research used resources of the National Energy Research Scientific Computing Center (NERSC), a U.S. Department of Energy Office of Science User Facility located at Lawrence Berkeley National Laboratory, operated under Contract No. DE-AC02-05CH11231 using NERSC Grant No. NP-ERCAP0021027, as well as computing resources on HAWK at the High-Performance Computing Center Stuttgart in project GWanalysis 44189. This material is based upon work supported by NSF's LIGO Laboratory, which is a major facility fully funded by the NSF. The authors gratefully acknowledge the Italian Istituto Nazionale di Fisica Nucleare (INFN), the French Centre National de la Recherche Scientifique (CNRS), and the Netherlands Organization for Scientific Research (NWO), for the construction and operation of the Virgo detector and the creation and support of the EGO consortium.

TABLE II. GW sampling parameters in GW170817 analysis. Most priors are uniform within given bounds. Luminosity distance $d_{\mathrm{L}}$ is uniform within a comoving volume of the specified radial dimension. The EOS prior is weighted by the ability to support mass constraints from high-mass pulsars, NICER observations, and the kilonova observations that suggested the formation of a hypermassive NS. The component mass prior indicates a constraint that is not used as a sampling parameter.

| parameter | symbol | prior bounds |
|---|---|---|
| Observational | | |
| Luminosity distance [Mpc] | $d_{\mathrm{L}}$ | 1, 75 |
| inclination | $\cos\theta_{JN}$ | $-1$, 1 |
| phase [rad] | $\phi$ | 0, $2\pi$ |
| polarization [rad] | $\psi$ | 0, $\pi$ |
| right ascension [rad] | $\alpha$ | 3.44616 (exact) |
| declination [rad] | $\delta$ | $-0.408084$ (exact) |
| Orbital | | |
| chirp mass [$\mathrm{M}_\odot$] | $\mathcal{M}$ | 1.18, 1.21 |
| mass ratio | $q$ | 0.125, 1 |
| component mass [$\mathrm{M}_\odot$] | $M_i$ | *>1.0* |
| aligned component spin | $\chi_i$ | $-0.15$, 0.15 |
| Hyper | | |
| Equation of State | EOS | 1, 3000 |

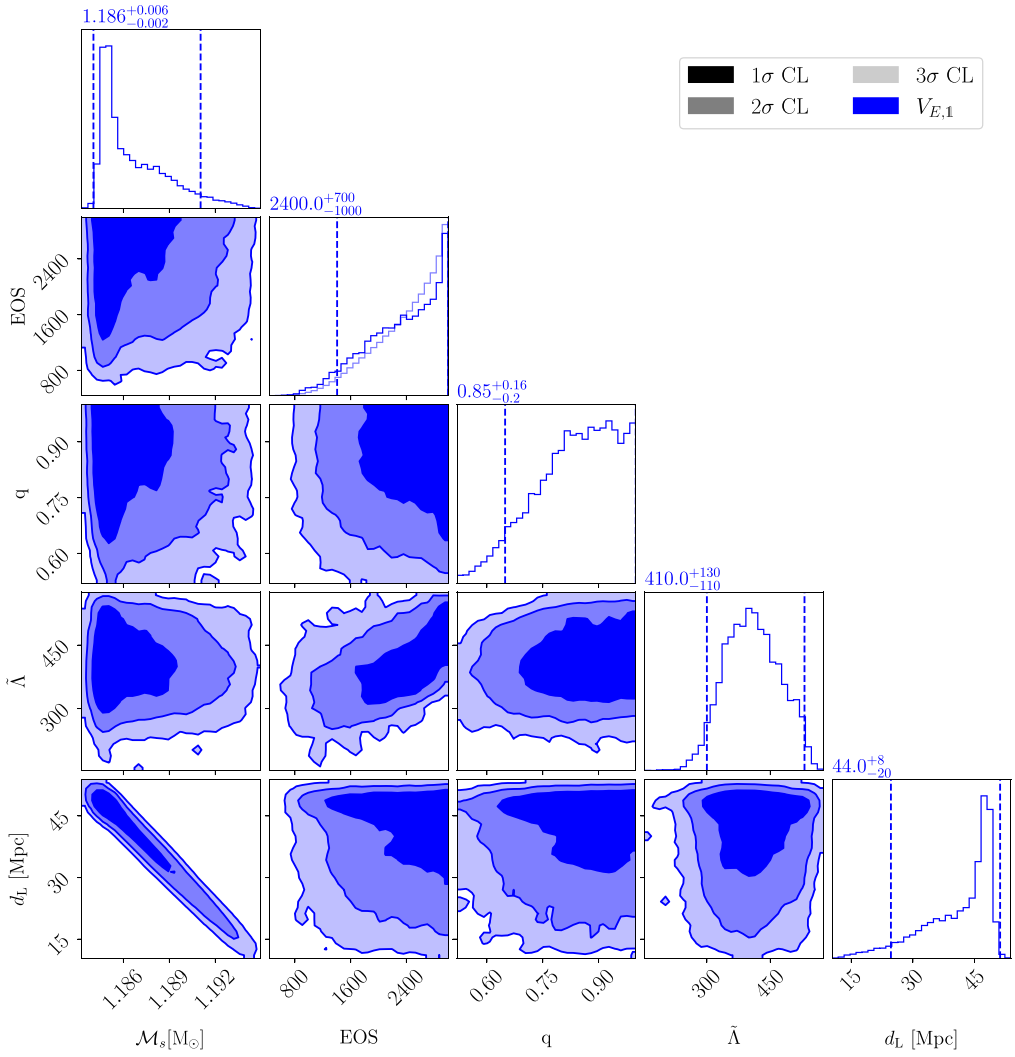


FIG. 5. Important system parameters for GW170817. We show a corner plot of (in reading direction) chirp mass, EOS index, mass ratio, tidal deformability, and luminosity distance. The blue contours represent the $V_{E,\mathbb{1}}$ recovery. A TPE recovery is not included because the low information gain in the EOS posterior (as indicated by the marginal deviation from the prior, shown in the corresponding histogram as a faint line) suggests that no constraints can be won. Dashed lines in the top histograms mark the 90% CI, and contours indicate $1\sigma$, $2\sigma$, and $3\sigma$ confidence levels in the 2D histograms.

## APPENDIX A: REANALYSIS OF GW170817

For a reanalysis of GW170817 [78], we use the available information on the gamma-ray burst afterglow and kilonova, motivating the modified prior distribution given in Table II. We also use a more informative EOS prior that is weighted by minimum mass constraints from precise pulsar observations [61–63,79], evidence for the formation of a hypermassive neutron star in the merger [70,71], and NICER analysis of millisecond pulsars [13–16]. Each measurement is assumed to be subject to Gaussian errors characterized by the respectively published uncertainty.

Figure 5 displays the recovered spread of several key parameters which are consistent with the original findings and recent reanalysis [5,80]. The luminosity distance peaks sharply near 46 Mpc, matching the spread in source chirp mass. This is slightly lower than originally reported. We can associate this effect with the wide spread of mass ratios, falling even below 0.6. The low mass ratios correspond to the extended prior range for the aligned spin components in comparison with Ref. [5] that considered the case $|\chi_i| < 0.05$. Since we find the spins (not shown) to deviate only slightly from the prior distribution and to be strongly anticorrelated, we conclude that there is no evidence for significant spin effects. The tidal deformability is relatively tightly constrained, falling way below the limits in nuclear-physics agnostic analysis of the original discovery [6,7,81] and matching findings of $80 \leqslant \tilde{\Lambda} \leqslant 580$ in a similar chiral EFT framework [29]. This is a prior-driven conclusion, though, and we find that the EOS distribution has hardly relaxed from the prior. This is due to the fact that GW170817 and chiral EFT up to $2\rho_{\mathrm{sat}}$ provide similar information on the EOS [82]. Since this run at the upper limit of plausible deformabilities is uninformative, no better constraints can be expected from a TPE

recovery on these data. This analysis does, therefore, suggest no preference for any particular realization of 3N interactions. Other GW detections with neutron stars have so far proven even less informative with respect to tidal effects. Further measurements of NS mergers are expected in the next observing runs, but current population models make it unlikely that these include signals that are considerably stronger than GW170817.

## APPENDIX B: COMPUTATION OF EVIDENCE

Equation (6) does not incorporate the fact that all neutron stars should be described by only one EOS. Including this knowledge leads to a slightly different expression for the resulting evidence:

$$\mathcal{Z} = \int \prod_{i=1}^{N} L_i(\theta_i, \mathrm{EOS}_i)\pi(\theta_i, \mathrm{EOS}_i) \times \delta(\mathrm{EOS}_i - \mathrm{EOS}_1)\, d\theta_i\, d\mathrm{EOS}_i \tag{B1}$$

$$= \int \prod_{i=1}^{N} L_i(\theta_i, \mathrm{EOS})\pi(\theta_i, \mathrm{EOS})\, d\theta_i\, d\mathrm{EOS} \tag{B2}$$

$$= \int \prod_{i=1}^{N} \mathcal{Z}_i p_i(\mathrm{EOS})\, d\mathrm{EOS} \tag{B3}$$

$$= \prod_{j=1}^{N} \mathcal{Z}_j \int \prod_{i=1}^{N} p_i(\mathrm{EOS})\, d\mathrm{EOS}. \tag{B4}$$

However, this prescription is misleading for the purpose of selecting among competing nuclear models. Consider, for instance, a segment of $\Lambda$ space at relatively low mass that is only approximately met by a single TPE EOS, whereas multiple $V_{E,\mathbb{1}}$ EOSs provide similarly good agreement with observations. This would naturally happen if $V_{E,\mathbb{1}}$ described the true EOS, independent of the total number of EOSs in each set. After some mergers with near-solar-mass NSs, Eq. (B4) would still suggest model preference for the inappropriate TPE description because it matches the expectation of a single true EOS better.

We see this effect in Fig. 6. The model preference in case of the TPE injection reduces massively. Even more prominent is the effect for the tenth event in case of the $V_{E,\mathbb{1}}$ injection. In our analysis, it leads to a reduction of the cumulative Bayes factor because of the distance overestimate which suggests lower component masses in the source frame. If, however, we include the demand that all observations should be explained by the same EOS, we observe that the same detection has the opposite effect. This traces back to the circumstance that this system contained the most massive primary star and the second highest chirp mass in our sample. It therefore probes a low $\Lambda$ regime that is not probed by other measurements. While the effects of a distance overestimate as discussed above favor the TPE model in this individual run, there are virtually no remaining TPE EOSs that agree decently with data from the lower-mass detections, too.

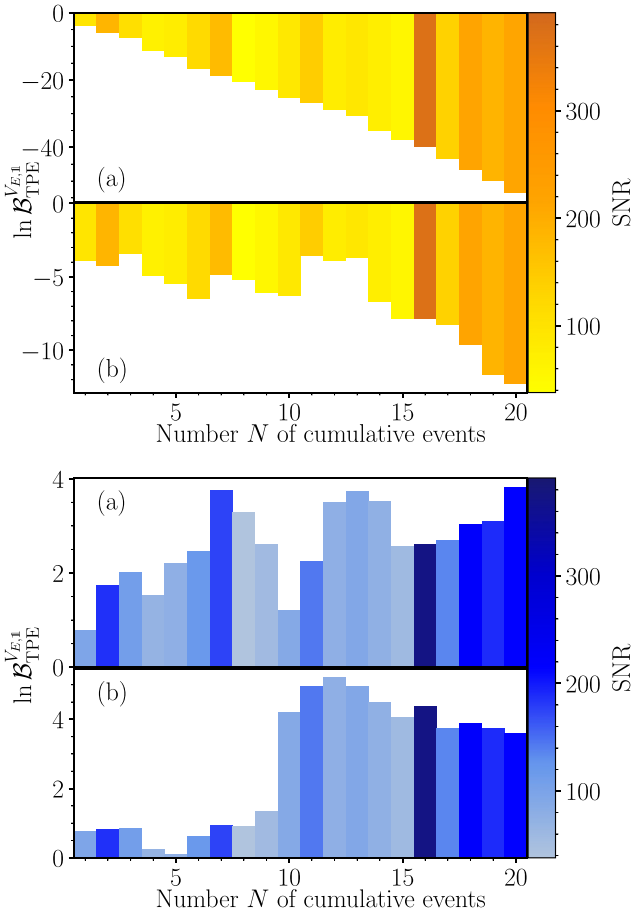


FIG. 6. Comparison of Bayes factors. Bayes factors as in Fig. 2, using Eq. (6) (a) and Eq. (B4) (b), respectively. Note the different scales. For the TPE (top) injection, the model preference becomes less decisive and the inclusion of some runs favors the $V_{E,\mathbb{1}}$ model when assuming that all observations result from the same EOS. For the $V_{E,\mathbb{1}}$ injection (bottom), the overall model preference remains nearly constant, while the contribution of some runs varies greatly.

[1] J. Lattimer and M. Prakash, Neutron star structure and the equation of state, Astrophys. J. **550**, 426 (2001).
[2] N. Chamel and P. Haensel, Physics of neutron star crusts, Living Rev. Relativ. **11**, 10 (2008).
[3] F. Özel and P. Freire, Masses, radii, and the equation of state of neutron stars, Annu. Rev. Astron. Astrophys. **54**, 401 (2016).
[4] S. Gandolfi, J. Lippuner, A. W. Steiner, I. Tews, X. Du, and M. Al-Mamun, From the microscopic to the macroscopic world: from nucleons to neutron stars, J. Phys. G **46**, 103001 (2019).
[5] B. P. Abbott *et al.* (Virgo, LIGO Scientific), GW170817: Observation of Gravitational Waves from a Binary Neutron Star Inspiral, Phys. Rev. Lett. **119**, 161101 (2017).
[6] B. P. Abbott *et al.* (Virgo, LIGO Scientific), GW170817: Measurements of Neutron Star Radii and Equation of State, Phys. Rev. Lett. **121**, 161101 (2018).

[7] B. P. Abbott *et al.* (LIGO Scientific, Virgo), Properties of the Binary Neutron Star Merger GW170817, Phys. Rev. X **9**, 011001 (2019).

[8] A. Bauswein, O. Just, H.-T. Janka, and N. Stergioulas, Neutron-star radius constraints from GW170817 and future detections, Astrophys. J. **850**, L34 (2017).

[9] D. Radice, A. Perego, F. Zappa, and S. Bernuzzi, GW170817: Joint constraint on the neutron star equation of state from multimessenger observations, Astrophys. J. **852**, L29 (2018).

[10] E. R. Most, L. R. Weih, L. Rezzolla, and J. Schaffner-Bielich, New Constraints on Radii and Tidal Deformabilities of Neutron Stars from GW170817, Phys. Rev. Lett. **120**, 261103 (2018).

[11] M. W. Coughlin, T. Dietrich, B. Margalit, and B. D. Metzger, Multimessenger Bayesian parameter inference of a binary neutron star merger, Mon. Not. R. Astron. Soc.: Letters **489**, L91 (2019).

[12] T. Dietrich, M. W. Coughlin, P. T. H. Pang, M. Bulla, J. Heinzel, L. Issa, I. Tews, and S. Antier, Multimessenger constraints on the neutron-star equation of state and the Hubble constant, Science **370**, 1450 (2020).

[13] T. E. Riley *et al.*, A *NICER* view of PSR J0030+0451: Millisecond pulsar parameter estimation, Astrophys. J. Lett. **887**, L21 (2019).

[14] M. C. Miller *et al.*, PSR J0030+0451 mass and radius from *NICER* data and implications for the properties of neutron star matter, Astrophys. J. Lett. **887**, L24 (2019).

[15] T. E. Riley *et al.*, A NICER view of the massive pulsar PSR J0740+6620 informed by radio timing and XMM-Newton spectroscopy, Astrophys. J. Lett. **918**, L27 (2021).

[16] M. C. Miller *et al.*, The radius of PSR J0740+6620 from NICER and XMM-Newton Data, Astrophys. J. Lett. **918**, L28 (2021).

[17] E. Epelbaum, H.-W. Hammer, and Ulf-G. Meissner, Modern theory of nuclear forces, Rev. Mod. Phys. **81**, 1773 (2009).

[18] R. Machleidt and D. R. Entem, Chiral effective field theory and nuclear forces, Phys. Rep. **503**, 1 (2011).

[19] T. Otsuka, T. Suzuki, J. D. Holt, A. Schwenk, and Y. Akaishi, Three-Body Forces and the Limit of Oxygen Isotopes, Phys. Rev. Lett. **105**, 032501 (2010).

[20] F. Wienholtz *et al.*, Masses of exotic calcium isotopes pin down nuclear forces, Nature (London) **498**, 346 (2013).

[21] B. D. Day, Nuclear saturation and nuclear forces, Comments Nucl. Part. Phys. (United Kingdom) **11**, 115 (1983).

[22] C. Drischler, K. Hebeler, and A. Schwenk, Chiral Interactions up to Next-to-Next-to-Next-to-Leading Order and Nuclear Saturation, Phys. Rev. Lett. **122**, 042501 (2019).

[23] D. Lonardoni, I. Tews, S. Gandolfi, and J. Carlson, Nuclear and neutron-star matter from local chiral interactions, Phys. Rev. Res. **2**, 022033(R) (2020).

[24] P. Navratil, S. Quaglioni, I. Stetcu, and B. R. Barrett, Recent developments in no-core shell-model calculations, J. Phys. G **36**, 083101 (2009).

[25] K. Hebeler, J. M. Lattimer, C. J. Pethick, and A. Schwenk, Equation of state and neutron star properties constrained by nuclear physics and observation, Astrophys. J. **773**, 11 (2013).

[26] J. E. Lynn, I. Tews, J. Carlson, S. Gandolfi, A. Gezerlis, K. E. Schmidt, and A. Schwenk, Quantum Monte Carlo calculations of light nuclei with local chiral two- and three-nucleon interactions, Phys. Rev. C **96**, 054007 (2017).

[27] M. Punturo, M. Abernathy, F. Acernese, B. Allen, N. Andersson *et al.*, The Einstein Telescope: A third-generation gravitational wave observatory, Class. Quantum Grav. **27**, 194002 (2010).

[28] S. Hild *et al.*, Sensitivity studies for third-generation gravitational wave observatories, Class. Quant. Grav. **28**, 094013 (2011).

[29] I. Tews, J. Margueron, and S. Reddy, Critical examination of constraints on the equation of state of dense matter obtained from GW170817, Phys. Rev. C **98**, 045804 (2018).

[30] K. E. Schmidt and S. Fantoni, A quantum Monte Carlo method for nucleon systems, Phys. Lett. B **446**, 99 (1999).

[31] J. Carlson, S. Gandolfi, F. Pederiva, S. C. Pieper, R. Schiavilla, K. E. Schmidt, and R. B. Wiringa, Quantum Monte Carlo methods for nuclear physics, Rev. Mod. Phys. **87**, 1067 (2015).

[32] J. E. Lynn, I. Tews, S. Gandolfi, and A. Lovato, Quantum monte carlo methods in nuclear physics: recent advances, Ann. Rev. Nucl. Part. Sci. **69**, 279 (2019).

[33] A. Gezerlis, I. Tews, E. Epelbaum, S. Gandolfi, K. Hebeler, A. Nogga, and A. Schwenk, Quantum Monte Carlo Calculations with Chiral Effective Field Theory Interactions, Phys. Rev. Lett. **111**, 032501 (2013).

[34] A. Gezerlis, I. Tews, E. Epelbaum, M. Freunek, S. Gandolfi, K. Hebeler, A. Nogga, and A. Schwenk, Local chiral effective field theory interactions and quantum Monte Carlo applications, Phys. Rev. C **90**, 054323 (2014).

[35] J. E. Lynn, I. Tews, J. Carlson, S. Gandolfi, A. Gezerlis, K. E. Schmidt, and A. Schwenk, Chiral Three-Nucleon Interactions in Light Nuclei, Neutron-$\alpha$ Scattering, and Neutron Matter, Phys. Rev. Lett. **116**, 062501 (2016).

[36] D. Lonardoni, S. Gandolfi, J. E. Lynn, C. Petrie, J. Carlson, K. E. Schmidt, and A. Schwenk, Auxiliary field diffusion Monte Carlo calculations of light and medium-mass nuclei with local chiral interactions, Phys. Rev. C **97**, 044318 (2018).

[37] K. Hebeler and A. Schwenk, Chiral three-nucleon forces and neutron matter, Phys. Rev. C **82**, 014314 (2010).

[38] L. Huth, I. Tews, J. E. Lynn, and A. Schwenk, Analyzing the fierz rearrangement freedom for local chiral two-nucleon potentials, Phys. Rev. C **96**, 054003 (2017).

[39] I. Tews, Spectrum of shear modes in the neutron-star crust: Estimating the nuclear-physics uncertainties, Phys. Rev. C **95**, 015803 (2017).

[40] A. Maselli, A. Sabatucci, and O. Benhar, Constraining three-nucleon forces with multimessenger data, Phys. Rev. C **103**, 065804 (2021).

[41] A. Sabatucci, O. Benhar, A. Maselli, and C. Pacilio, Sensitivity of neutron star observations to three-nucleon forces, Phys. Rev. D **106**, 083010 (2022).

[42] K. Chatziioannou, Neutron star tidal deformability and equation of state constraints, Gen. Rel. Grav. **52**, 109 (2020).

[43] T. Hinderer, Tidal Love numbers of neutron stars, Astrophys. J. **677**, 1216 (2008).

[44] I. Tews, T. Krüger, K. Hebeler, and A. Schwenk, Neutron Matter at Next-to-Next-to-Next-to-Leading Order in Chiral Effective Field Theory, Phys. Rev. Lett. **110**, 032504 (2013).

[45] T. Krüger, I. Tews, K. Hebeler, and A. Schwenk, Neutron matter from chiral effective field theory interactions, Phys. Rev. C **88**, 025802 (2013).

[46] F. Acernese *et al.* (VIRGO), Advanced Virgo: a second-generation interferometric gravitational wave detector, Class. Quantum Grav. **32**, 024001 (2015).

[47] J. Aasi *et al.* (LIGO Scientific), Advanced LIGO, Class. Quant. Grav. **32**, 115012 (2015).

[48] R. Abbott *et al.* (LIGO Scientific, VIRGO, KAGRA), GWTC-3: Compact Binary Coalescences Observed by LIGO and Virgo During the Second Part of the Third Observing Run, arXiv:2111.03606 (2021).

[49] R. Abbott *et al.* (LIGO Scientific, VIRGO), GWTC-2.1: Deep Extended Catalog of Compact Binary Coalescences Observed by LIGO and Virgo During the First Half of the Third Observing Run, arXiv:2108.01045 (2021).

[50] P. Petrov, L. P. Singer, M. W. Coughlin, V. Kumar, M. Almualla, S. Anand, M. Bulla, T. Dietrich, F. Foucart, and N. Guessoum, Data-driven expectations for electromagnetic counterpart searches based on LIGO/Virgo public alerts, Astrophys. J. **924**, 54 (2022).

[51] A. Colombo, O. S. Salafia, F. Gabrielli, G. Ghirlanda, B. Giacomazzo, A. Perego, and M. Colpi, Multi-messenger observations of binary neutron star mergers in the o4 run, Astrophys. J. **937**, 79 (2022).

[52] C. Pacilio, A. Maselli, M. Fasano, and P. Pani, Ranking Love Numbers for the Neutron Star Equation of State: The Need for Third-Generation Detectors, Phys. Rev. Lett. **128**, 101101 (2022).

[53] D. Reitze *et al.*, Cosmic explorer: the U.S. contribution to gravitational-wave astronomy beyond LIGO, Bulletin of the AAS **51**, 035 (2019).

[54] R. Abbott *et al.* (LIGO Scientific, VIRGO, KAGRA), The population of merging compact binaries inferred using gravitational waves through GWTC-3, arXiv:2111.03634 (2021).

[55] I. Mandel and F. S. Broekgaarden, Rates of compact object coalescences, Living Rev. Rel. **25**, 1 (2022).

[56] K. Stovall *et al.*, PALFA discovery of a highly relativistic double neutron star binary, Astrophys. J. **854**, L22 (2018).

[57] M. Burgay, N. D'Amico, A. Possenti, R. Manchester, A. Lyne, *et al.*, An increased estimate of the merger rate of double neutron stars from observations of a highly relativistic system, Nature (London) **426**, 531 (2003).

[58] J. G. Martinez, K. Stovall, P. C. C. Freire, J. S. Deneva, F. A. Jenet, M. A. McLaughlin, M. Bagchi, S. D. Bates, and A. Ridolfi, Pulsar J0453+1559: A double neutron star system with a large mass asymmetry, Astrophys. J. **812**, 143 (2015).

[59] Y. Suwa, T. Yoshida, M. Shibata, H. Umeda, and K. Takahashi, On the minimum mass of neutron stars, Mon. Not. R. Astron. Soc. **481**, 3305 (2018).

[60] T. Dietrich, A. Samajdar, S. Khan, N. K. Johnson-McDaniel, R. Dudi, and W. Tichy, Improving the NRTidal model for binary neutron star systems, Phys. Rev. D **100**, 044003 (2019).

[61] J. Antoniadis, P. C. Freire, N. Wex, T. M. Tauris, R. S. Lynch, *et al.*, A massive pulsar in a compact relativistic binary, Science **340**, 1233232 (2013).

[62] Z. Arzoumanian *et al.* (NANOGrav), The NANOGrav 11-year data set: High-precision timing of 45 millisecond pulsars, Astrophys. J. Suppl. **235**, 37 (2018).

[63] E. Fonseca *et al.*, Refined mass and geometric measurements of the high-mass PSR J0740+6620, Astrophys. J. Lett. **915**, L12 (2021).

[64] R. Smith, S. E. Field, K. Blackburn, C.-J. Haster, M. Pürrer, V. Raymond, and P. Schmidt, Fast and accurate inference on gravitational waves from precessing compact binaries, Phys. Rev. D **94**, 044031 (2016).

[65] J. Skilling, Nested sampling for general Bayesian computation, Bayesian Analysis **1**, 833 (2006).

[66] E. Thrane and C. Talbot, An introduction to Bayesian inference in gravitational-wave astronomy: Parameter estimation, model selection, and hierarchical models, Publ. Astron. Soc. Austral. **36**, e010 (2019).

[67] R. J. E. Smith, G. Ashton, A. Vajpeyi, and C. Talbot, Massively parallel Bayesian inference for transient gravitational-wave astronomy, Mon. Not. R. Astron. Soc. **498**, 4492 (2020).

[68] G. Ashton *et al.*, BILBY: A user-friendly Bayesian inference library for gravitational-wave astronomy, Astrophys. J. Suppl. **241**, 27 (2019).

[69] T. Dietrich, T. Hinderer, and A. Samajdar, Interpreting binary neutron star mergers: describing the binary neutron star dynamics, modelling gravitational waveforms, and analyzing detections, Gen. Rel. Grav. **53**, 27 (2021).

[70] L. Rezzolla, E. R. Most, and L. R. Weih, Using gravitational-wave observations and quasi-universal relations to constrain the maximum mass of neutron stars, Astrophys. J. **852**, L25 (2018).

[71] B. Margalit and B. D. Metzger, Constraining the maximum mass of neutron stars from multi-messenger observations of GW170817, Astrophys. J. Lett. **850**, L19 (2017).

[72] M. Shibata, E. Zhou, K. Kiuchi, and S. Fujibayashi, Constraint on the maximum mass of neutron stars using GW170817 event, Phys. Rev. D **100**, 023015 (2019).

[73] M. Ruiz, S. L. Shapiro, and A. Tsokaros, GW170817, general relativistic magnetohydrodynamic simulations, and the neutron star maximum mass, Phys. Rev. D **97**, 021501(R) (2018).

[74] N. Kunert, P. T. H. Pang, I. Tews, M. W. Coughlin, and T. Dietrich, Quantifying modeling uncertainties when combining multiple gravitational-wave detections from binary neutron star sources, Phys. Rev. D **105**, L061301 (2022).

[75] T. M. Tauris *et al.*, Formation of double neutron star systems, Astrophys. J. **846**, 170 (2017).

[76] B. Abbott *et al.* (LIGO Scientific, Virgo), GW190425: observation of a compact binary coalescence with total mass $\sim 3.4 M_{\odot}$, Astrophys. J. Lett. **892**, L3 (2020).

[77] S. Galaudage, C. Adamcewicz, X.-J. Zhu, S. Stevenson, and E. Thrane, Heavy double neutron stars: birth, midlife, and death, Astrophys. J. Lett. **909**, L19 (2021).

[78] R. Abbott *et al.* (LIGO Scientific, Virgo), Open data from the first and second observing runs of Advanced LIGO and Advanced Virgo, SoftwareX **13**, 100658 (2021).

[79] R. W. Romani, D. Kandel, A. V. Filippenko, T. G. Brink, and W. Zheng, Psr j0952-0607: The fastest and heaviest known galactic neutron star, Astrophys. J. Lett. **934**, L17 (2022).

[80] T. Narikawa and N. Uchikata, Follow-up analyses of the binary-neutron-star signals GW170817 and GW190425 by using post-Newtonian waveform models, Phys. Rev. D **106**, 103006 (2022).

[81] S. De, D. Finstad, J. M. Lattimer, D. A. Brown, E. Berger, and C. M. Biwer, Tidal Deformabilities and Radii of Neutron Stars from the Observation of GW170817, Phys. Rev. Lett. **121**, 091102 (2018).

[82] C. D. Capano, I. Tews, S. M. Brown, B. Margalit, S. De, S. Kumar, D. A. Brown, B. Krishnan, and S. Reddy, Stringent constraints on neutron-star radii from multimessenger observations and nuclear theory, Nat. Astron. **4**, 625 (2020).